Modeling FMCW Radar for Subsurface Analysis

Sigurd Eide, Titus Casademont, Øyvind Lund Aardal, and Svein-Erik Hamran

***Abstract*—Determining subsurface properties through ground penetrating radar sounding can be challenging, especially in planetary exploration, where little is known about the terrain and additional observations are limited. Analysis and interpretation of data acquired with the Radar Imager for Mars' Subsurface Experiment (RIMFAX) could therefore be improved by in-detail comparison with forward modeling. RIMFAX transmits a frequency modulated continuous waveform and utilizes a stretch processing receiver, and we demonstrate how accurate modeling can be achieved through finite-difference time-domain simulations. As the simulation scheme do not allow for direct implementation of such radar system, this study presents the necessary steps in order to replicate the same transmitter and receiver characteristics. In particular, we investigate how the method holds for modeling sounding in a realistic subsurface medium with attenuating and dispersive properties, by comparing the results with analytical estimates. The modeling approach is also assessed through comparison with RIMFAX field test measurements.**

***Index Terms*—Finite-difference time-domain (FDTD), frequency modulated continuous wave (FMCW), ground penetrating radar (GPR), Radar Imager for Mars' Subsurface Experiment (RIMFAX).**

I. Introduction

IMAGING of geological layering and analysis of subsurface properties are among the principal applications of ground penetrating radar (GPR). In planetary exploration, means of constraining acquired GPR data are limited to surface observations, either from orbital imagery or by other payload instruments. This can be difficult and ultimately lead to controversy surrounding the results, as to whether actual subsurface structures have been detected or if it is rather system noise being misinterpreted [1], [2]. Additional insight can be obtained, however, by testing hypotheses and comparing with modeling, e.g., evaluating how the subsurface have affected reflection geometries and target responses in recorded radargrams. Forward modeling has been done in lunar exploration to assess interpreted subsurface model and electromagnetic media properties [3], as well as to assure adequate processing of acquired data [4]. Accordingly, modeling studies could be helpful for analyzing soundings from the Radar Imager for Mars' Subsurface Experiment (RIMFAX) [5] on the Perseverance rover mission, the first GPR to be operating from the surface of Mars.

In order to use modeling for analyzing subsurface properties, modeling should be able to reproduce the same spectral characteristics and target responses as would be acquired with the transmitter and receiver of a specific GPR system. RIMFAX is a frequency modulated continuous wave (FMCW) radar with a stretch processing receiver, operating in the 150–1200 MHz frequency range (see Hamran *et al.* [5] for detailed information about the instrument and acquisition modes). Among several modeling approaches [6], the finite-difference time-domain (FDTD) method has been largely adapted by the GPR-community with availability of open-source software [7]. For modeling pulsed radar systems, FDTD-simulations are excited by a copy of the transmitted waveform and reflections from the subsurface model are recorded. But this is not viable for FMCW radars due to high computational costs, as the duration of a FMCW sweep can be on the order of 100–1000 times longer than the waveform in pulsed radar. To the best of our knowledge, FMCW-implementation in FDTD has not previously been thoroughly investigated.

In this study, we demonstrate how the target response of RIMFAX and other FMCW stretch processing receivers can be obtained through FDTD-simulations and subsequent corrections, asserting that modeling can be used for in-detail subsurface analysis. The obstacle of long sweep times is overcome by conducting simulations with a short-duration broadband waveform and afterwards correcting for differences in the waveform frequency spectra, as well as incorporating effects due to antenna gain and receiver processing. This can be accomplished because acquisition, the subsurface model and receiver processing can be described in a linear time-invariant system, as described in the method section. Notably, we present modeling of radar sounding in realistic media with attenuation and dispersion properties, and verify the results by comparing with analytical estimates. Assessment of the modeling approach is also done through comparison with RIMFAX field test measurements.

II. Method

The method is subdivided into four sections. Section A describe the FMCW signal, Section B the FMCW stretch processing receiver, and Section C the FDTD-modeling corrections. Last, in Section D, an example demonstrates how FDTD-simulations with a short-duration broadband waveform are corrected to reproduce the same time domain result as a that of a long duration FMCW and a stretch processing receiver.

Manuscript received October 4, 2021; revised December 6, 2021 and January 31, 2022; accepted March 22, 2022. Date of publication April 5, 2022; date of current version April 27, 2022. *(Corresponding author: Sigurd Eide.)*

Sigurd Eide, Titus Casademont, and Svein-Erik Hamran are with the Department of Technology Systems, University of Oslo, 2007 Kjeller, Norway (e-mail: sigurd.eide@its.uio.no; titus.casademont@its.uio.no; s.e.hamran@its.uio.no).

Øyvind Lund Aardal is with the Department of Technology Systems, University of Oslo, 2007 Kjeller, Norway, and also with the Norwegian Defence Research Establishment (FFI), 2027 Kjeller, Norway (e-mail: o.l.aardal@its.uio.no).

Digital Object Identifier 10.1109/JSTARS.2022.3165135

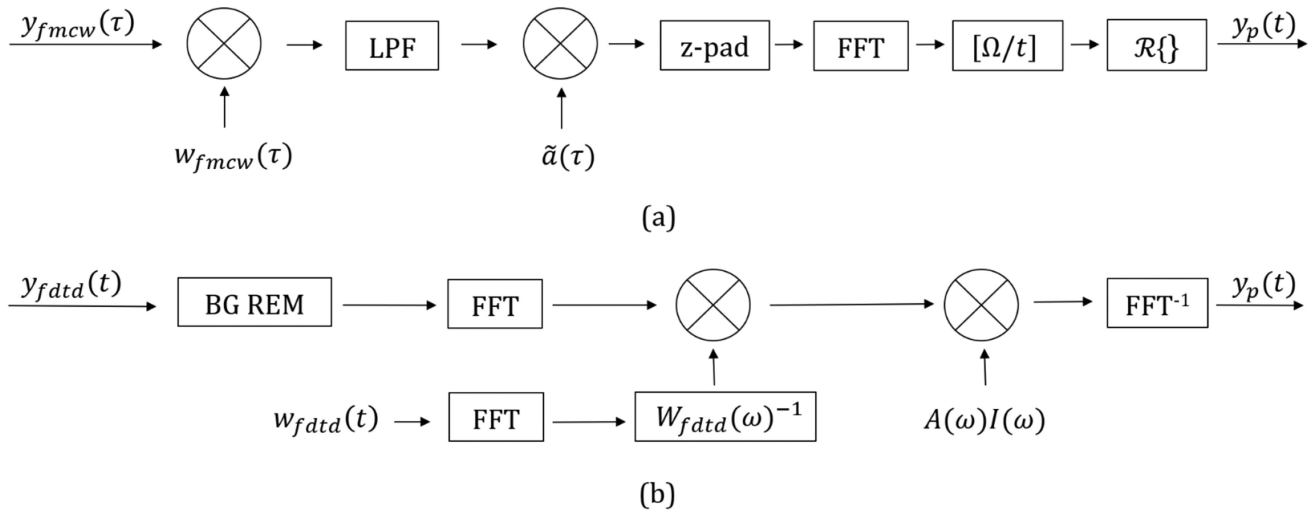

Fig. 1. Block diagrams of (a) stretch processing receiver and (b) FDTD-modeling corrections. Crossed circles indicate mixing or multiplication (not distinguishing between analog and digital operations). "LPF" is low pass filtering and "z-pad" is zero-padding/time-shifting. "FFT" and "FFT^{-1}" is the forward and inverse Fast Fourier Transform. $[\Omega/t]$ indicates variable substitution and $\Re\{\}$ symbolizes the operation of taking the real value of a complex signal. Background removal of FDTD-source effects is represented by "BG REM," while $W_{\text{fdtd}}(\omega)^{-1}$ is the deconvolution operator in frequency domain. Variables are as described in the text.

A. FMCW Signal

A linearly varying FMCW with start angular frequency Ω_0, bandwidth B, and sweep length T, can be written as

$$w_{\text{fmcw}}(\tau) = \tilde{i}(\tau) \exp j \left[\Omega_0 \tau + \pi \frac{B}{T} \tau^2\right]. \tag{1}$$

The exponential term, containing the waveform oscillation, is multiplied with an instrument-specific correction term $\tilde{i}(\tau)$ that describes amplitude variations with frequency in the radiated signal. We refer to the time variable τ as "sweep-time," which is related to the timing during instrument acquisition.

Received reflections from N targets with two-way travel-time delays t_i are then written

$$y_{\text{fmcw}}(\tau) = \tilde{i}(\tau) \sum_{i=1}^{N} d_i \tilde{h}_i(\tau) \exp j \left[\Omega_0(\tau - t_i) + \pi \frac{B}{T}(\tau - t_i)^2\right] \tag{2}$$

where d_i is assumed frequency independent and corrects the amplitude for geometrical spreading and the target's radar cross section. For propagation in attenuating and dispersive media, reflected signals will besides have undergone frequency dependent alteration [8]–[10], here represented by the term $\tilde{h}_i(\tau)$ in sweep-time domain.

B. Stretch Processing Receiver

A stretch processing receiver as illustrated in Fig. 1(a), takes the received signal in (2) and conducts several operations to output a compressed result, i.e., the target responses. First, the received signal is mixed with the transmitted waveform and the product is passed through a low pass filter. These operations produce the deramped signal [11]

$$y_{dr}(\tau) = \tilde{i}(\tau) \sum_{i=1}^{N} d_i \tilde{h}_i(\tau) \exp j \left[2\pi \frac{B}{T} t_i \tau - \theta_i\right] \tag{3}$$

where each target introduces a constant phase shift

$$\theta_i = -\Omega_0 t_i + \pi B t_i^2 / T \approx -\Omega_0 t_i \,. \tag{4}$$

The term $\pi B t_i^2/T$ is known as the "residual video phase" and has a very small contribution. It is typical negligible in subsurface sounding where target delay times are relatively short compared to sweep lengths, as $\pi B t_i^2/T\Omega_0 t_i \propto t_i/T \approx 0$.

The resultant deramped signal consists of "separate tones" denoted beat frequencies, $\Omega_b = 2\pi B t_i/T$, which correspond to the two-way travel-time delay t_i of each reflection. This principle is illustrated in Fig. 2 for a single reflection.

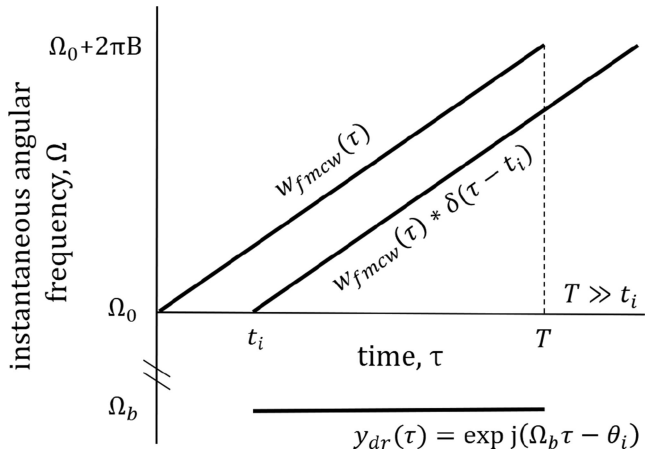

Fig. 2. Illustration of stretch processing and beat-frequency for a single reflection at t_i, where the reflected signal is a time-delayed copy of the transmitted waveform. $\delta(\tau)$ is the Dirac delta function.

By zero-padding the beginning of the mixer output, effectively time-shifting the signal, the constant phase term (4) can be removed

$$y_{dr}(\tau) * \delta(\tau - t_s) = \tilde{i}(\tau) \sum_{i=1}^{N} d_i \tilde{h}_i(\tau) \exp j\left[\Omega_b(\tau - t_s) - \theta_i\right] = \tilde{i}(\tau) \sum_{i=1}^{N} d_i \tilde{h}_i(\tau) \exp j\left[\Omega_b \tau\right]. \tag{5}$$

We describe this through convolution ($*$) with the Dirac delta function and an appropriately chosen time shift, $t_s = \Omega_0 T/2\pi B$.

Before zero-padding and transforming the mixer-output into frequency domain, an amplitude taper $\tilde{a}(\tau)$ is included to modify the target responses, lowering sidelobes at the cost of a broader mainlobe and reduced signal-to-noise ratio. It should be noted that there are options on how to apply this taper that could end up distorting the target responses, though negligible when FMCW sweep times are much longer than the target delays [11].

Employing that multiplication in time domain equals convolution in frequency domain, the Fourier transform of the product then yields

$$\begin{aligned} Y_{dr,a}(\Omega) &= \int_{-\infty}^{\infty} \tilde{a}(\tau) y_{dr}(\tau - t_s) e^{-j\Omega\tau}\, d\tau \\ &= \tilde{A}(\Omega) * \int_{-\infty}^{\infty} y_{dr}(\tau - t_s) e^{-j\Omega\tau}\, d\tau \\ &= \tilde{A}(\Omega) * \tilde{I}(\Omega) \; * \int_{-\infty}^{\infty} \sum_{i=1}^{N} d_i \tilde{h}_i(\tau) e^{j\Omega_b\tau} e^{-j\Omega\tau}\, d\tau \\ &= \tilde{A}(\Omega) * \tilde{I}(\Omega) \; * \sum_{i=1}^{N} d_i \tilde{H}_i(\Omega) * \int_{-\infty}^{\infty} e^{j(\Omega_b - \Omega)\tau}\, d\tau\,. \end{aligned} \tag{6}$$

The integral term is evaluated over the interval $[0, T]$, yielding a scaled sinc function plus an imaginary term $\zeta(t_i, \Omega)$

$$\int_0^T e^{j(2\pi \frac{B}{T} t_i - \Omega)\tau}\, d\tau = T \frac{\sin\left[\pi(2Bt_i - \frac{\Omega T}{\pi})\right]}{\pi(2Bt_i - \frac{\Omega T}{\pi})} + \zeta(t_i, \Omega) \tag{7}$$

so that

$$Y_{dr,a}(\Omega) = \tilde{A}(\Omega) * \tilde{I}(\Omega) * T \sum_{i=1}^{N} d_i \tilde{H}_i(\Omega) * \left[\operatorname{sinc}\left(2Bt_i - \frac{\Omega T}{\pi}\right) + \zeta(t_i, \Omega)\right]. \tag{8}$$

Since each beat-frequency is related to the travel-time delay, or corresponding target range, the frequency in (8) can be substituted with time through a linear relationship

$$\Omega = 2\pi \frac{B}{T} t\,. \tag{9}$$

This time variable is written as t and termed "fast-time". It has been discriminated from the sweep-time τ that span the frequency sweep during acquisition, as fast-time is on a much shorter time scale similar to the travel-time delays. The frequency variables in sweep-time can therefore be redefined to time variables in fast-time ($\tilde{I}[\Omega(t)] = i(t)$, $\tilde{A}[\Omega(t)] = a(t)$, $\tilde{H}_i[\Omega(t)] = h_i(t)$, and $\zeta[t_i, \Omega(t)] = \zeta(t_i, t)$)

$$Y_{dr,a}[\Omega(t)] = a(t) * i(t) * T \sum_{i=1}^{N} d_i h_i(t) * [\operatorname{sinc}[2B(t - t_i)] + \zeta(t_i, t)] \tag{10}$$

where we take advantage of sinc being an even function.

The signal in (10) is complex, so we define the final processed recording as its real part, $y_p(t) = \Re\{Y_{dr,a}[\Omega(t)]\}$. The expression can be simplified using the Dirac delta function and defining the reflectivity series

$$\begin{aligned} &T \sum_{i=1}^{N} d_i h_i(t) * \operatorname{sinc}[2B(t - t_i)] \\ &\quad = T \operatorname{sinc}(2Bt) * \sum_{i=1}^{N} d_i \delta(t - t_i) * h_i(t) \\ &\quad = T \operatorname{sinc}(2Bt) * r(t) \\ &\quad = T\, r(t)\,. \end{aligned} \tag{11}$$

The reflectivity series $r(t)$ is the typical definition for reflections in attenuating and dispersive media, employing the nonstationary convolution model [12]. The sinc function can furthermore be safely ignored as the convolution will not alter the expression, because the waveform's frequency sweep in (1) is contained within $2B$.

The final result is expressed in terms of a convolution model between the amplitude taper, instrument-correction, and reflectivity series in fast-time, or as multiplication of corresponding spectra in frequency domain:

$$\begin{aligned} y_p(t) &= a(t) * i(t) * T\, r(t) \\ Y_p(\omega) &= A(\omega)\, I(\omega)\, T\, R(\omega)\,. \end{aligned} \tag{12}$$

As seen in the equations above, the results are scaled by a factor T, the instrument sweep length. Note also that ω is the fast-time frequency, which is distinguished from the sweep-time frequency Ω in (6)–(9). In Fig. 3, the variables are presented in both sweep-time and fast-time, through the linear relation described in (9). Also presented are a RIMFAX-specific instrument correction and a commonly used amplitude taper.

C. FDTD-Modeling Corrections

In this section, we will review FDTD-simulations and the necessary corrections steps so that one may obtain the same results as a FMCW radar. The raw simulation results $y_{\text{fdtd}}(t)$ can be described as the convolution between the short-duration excitation waveform $w_{\text{fdtd}}(t)$ and the subsurface model's reflectivity series $r(t)$. Additionally, an inevitable direct wave between source and receiver will be included together with a term $\gamma_w(t)$ describing source excitation effects [13]

$$y_{\text{fdtd}}(t) = w_{\text{fdtd}}(t) * [r(t) + d_d \delta(t - t_d)] + \gamma_w(t)\,. \tag{13}$$

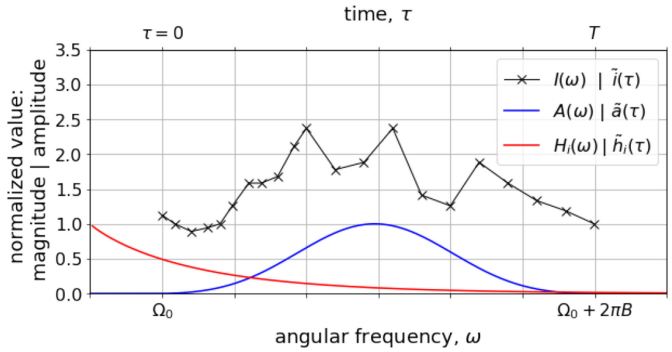

Fig. 3. Instrument correction (black) and amplitude taper (blue) in fast-time frequency domain and sweep-time time domain. Normalized magnitude is used in frequency domain representation and normalized amplitude is used in time domain representation. The instrument correction is assumed to be equal the measurements of RIMFAX' bore-sight gain [5], while the amplitude taper is a commonly used blackman window. Also plotted is an example of an attenuation and dispersion functions (red), accounting for the frequency dependent attenuation for an individual reflection. The function equals that of a constant-Q medium, as described in "Results and Discussion" Section A.

Here, $r(t)$ is the same as in (11), d_d corrects the amplitude of the direct wave for geometrical spreading and t_d is the travel-time of the direct wave.

In Fig. 1(b) a block diagram of the modeling corrections is presented. In order to model a monostatic radar system, the first operation is a background removal, subtracting the simulation over the subsurface model with, e.g., a subtrahend containing the direct wave and source effects

$$y_{\text{fdtd}}(t) - [d_d w_{\text{fdtd}}(t - t_d) + \gamma_w(t)] = w_{\text{fdtd}}(t) * r(t). \quad (14)$$

The background subtrahend could typically be another simulation conducted over an empty model. Depending on the focus of the study, the background removal could alternatively be conducted with a trend extracted from the simulated data similar to standard techniques in field data processing.

When studying air-coupled radars with a focus on weak subsurface reflections, it can be beneficial to include the surface reflection in the subtrahend. First, it is an efficient way of eliminating artificial "ringing" between the surface reflection and insufficiently damped reflections from the bounding sides of the FDTD-model. Second, if the radar system's waveform have dominant sidelobes, they could drown out weaker reflections, which is especially relevant for subsurface reflections in attenuating media.

By using the waveform to deconvolve the remainder in (14), the transmitted waveform is effectively removed from the signal. This operation is achieved through multiplication in frequency domain with the inverse of the waveform spectrum,

$$W_{\text{fdtd}}^{-1}(\omega) W_{\text{fdtd}}(\omega) R(\omega) = R(\omega) \quad (15)$$

where

$$W_{\text{fdtd}}^{-1}(\omega) = W_{\text{fdtd}}^{*}(\omega) / |W_{\text{fdtd}}(\omega)|^2 . \quad (16)$$

The frequency ω is equivalent to the fast-time frequency in stretch processing.

The next step is multiplication with an instrument correction $I(\omega)$ and amplitude taper $A(\omega)$. In time domain, the result is the same as in (12), but with an unscaled reflectivity series

$$y_p(t) = a(t) * i(t) * r(t) . \quad (17)$$

Since this result, equal the output form a FMCW receiver, we have demonstrated that it is possible to conduct FDTD-simulations with a short-duration waveform and obtain the same response as that of a FMCW radar with long sweep time.

D. Modeling Example

To illustrate how the correction steps modify a FDTD-simulation, in Fig. 4 modeling over a no-loss planar, multilayered model is compared to the equivalent FMCW response. The simple geometry in (a) allows for calculating a 1D-reflectivity series and the FMCW response according to (12), as presented in (b). The amplitude taper $A(\omega)$ and instrument correction $I(\omega)$ are as in Fig. 3.

Some considerations are needed in order to model acquisition similar to that of RIMFAX, which has a monostatic air-coupled antenna elevated 0.6 m off the surface. The source–receiver offset in (a) is necessary for the receiver cell to be uninfluenced by the source [7], so these are offset by 0.4 m from one another and located inside the uppermost layer (with permittivity equal that of air, $\epsilon' = 1$). The source and receiver are also elevated 0.57 m above the second layer ($\epsilon' = 4.1$), calculated from the straight ray-path to the central midpoint on that surface ($0.57 = \sqrt{0.6^2 - (0.4/2)^2}$). The waveform in Fig. 4(c) is a Gaussian-modulated sine-wave with centre frequency (675 MHz) and bandwidth (1050 MHz), chosen to have a short-duration that keep computation times low while its frequency spectra encompasses the bandwidth of RIMFAX. Source excitation is done with a Hertzian dipole polarized in the *x*-direction.

In (d) are the uncorrected FDTD-simulations, source artifacts, the results after background removal, and the final corrected modeling results. FDTD-simulations are conducted with the open-source software gprMax [8] within requirements for a stable simulation, with spatial discretization of 0.01 m and a time increment equal 1.92583e-11 s. Not shown in the model in (a) are the 15 cells thick "perfectly matched layers" at all sides of the model, limiting reflections at the model boundaries.

In the uncorrected FDTD-simulations in (d), the reflection from the second layer is partially obscured by the direct wave, but through background removal it can be recovered. The background subtrahend in this example is the results from simulations conducted over an empty model. By comparing the FMCW response in (b) and the modeling results in (d), it can be seen that modeling corrections give the same results as would be obtained by a FMCW radar, despite there are some minor differences between the 1-D and 3-D reflectivity series. The 3-D model used in FDTD-simulations will also include multiples from within the layers, as well as potential ringing from inadequately damped model boundary reflections.

III. Results and Discussion

The results and discussion is divided into three sections. Section A presents the theory of propagation in attenuating and dispersive media, and its implementation in FDTD-simulations.

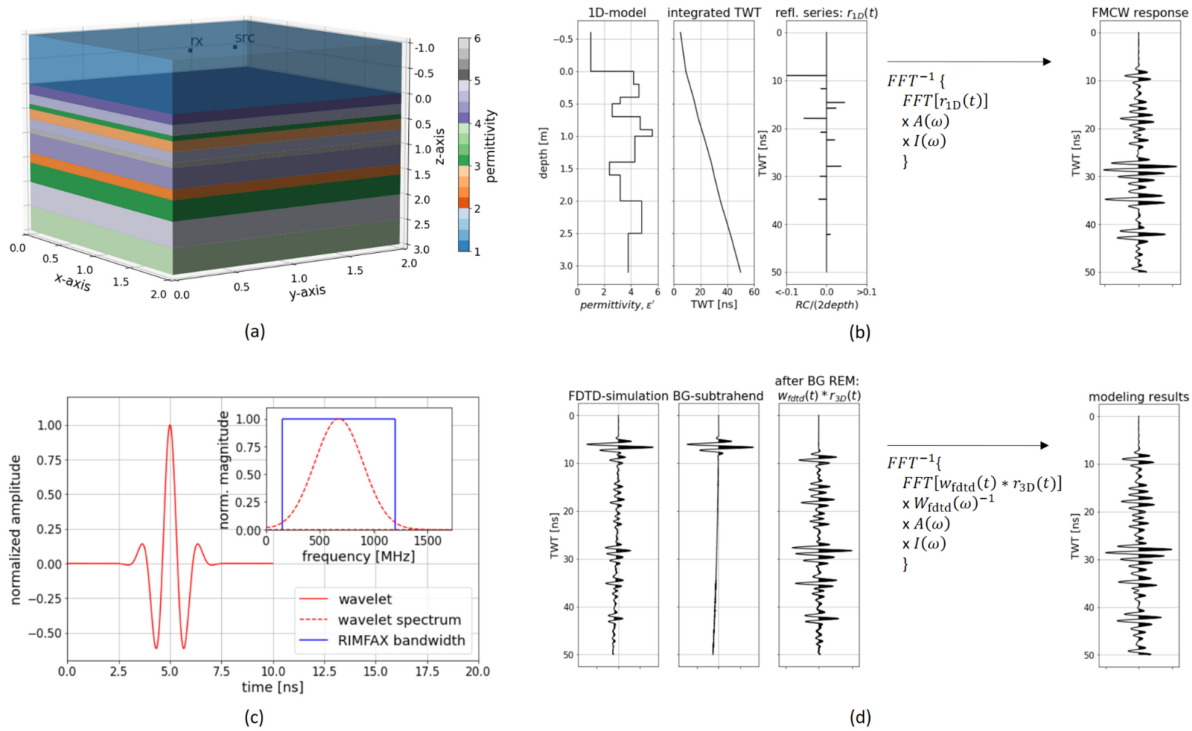

Fig. 4. FDTD-modeling corrections for a no-loss planar, multi-layer model, and the equivalent FMCW response. (a) 3D permittivity model. Not shown in figure are the absorbing boundary conditions applied at all faces of the model space to constrain artificial reflections. (b) 1D-equivalent permittivity model, integrated two-way travel-time (TWT), reflectivity series and analytical FMCW response. The integrated travel-time is calculated according to the permittivity with depth (TWT $= 2$ depth $\sqrt{\varepsilon'}/c$, with c being the speed of light). The corresponding reflectivity series $r(t)$ is equal the reflection constant (RC) at each change in permittivity, multiplied with an amplitude correction of $1/(2 \text{ depth})$ according to geometrical spreading and reflections at planar interfaces. Scaling of the reflectivity series as in (11) is ignored. The FMCW response is obtained from multiplication in frequency domain according to (12). For display purposes, the wiggle-trace has been multiplied with t^2 as a gain function. (c) Gaussian-modulated sine-wave used to excite FDTD-simulations. Next to the waveform's spectrum, RIMFAX' bandwidth is also included for reference. (d) Uncorrected FDTD-simulations, source artifacts (BG-subtrahend), the results after background removal, and the corrected modeling results. Wiggle-traces are displayed with a t^2 gain.

A comparison between modeling results and analytical estimates is presented in Section B, where also the accuracy of the modeling approach is discussed. In Section C, a RIMFAX field test radargram is compared with forward modeling along the same acquisition line. Here, we assess how well modeling reproduce the field recordings, as well as how forward modeling can verify subsurface properties, demonstrating potential use in radargram analysis.

A. *Modeling in Attenuating and Dispersive Media*

To assess how the presented method holds for modeling the GPR response over a subsurface with realistic properties, we study propagation in an attenuating and dispersive media. This is likely also a representative description for Martian rocks and regolith, where dielectric models have been presented based on measurement of electric and magnetic properties in analog lithologies [14], [15]. We will focus on a constant-Q medium, originally used to describe the cumulative attenuating effects for seismic waves [16], but which has also been found applicable for describing microwave propagation in natural soils and rocks over the GPR frequency range (0.1–1.0 GHz) [8], [9].

Bano [10] demonstrated that the "universal" power-law [17], which approximates media permittivities above the relaxation frequency, corresponds to a constant-Q model

$$\frac{\Im}{\Re}\{\varepsilon(\omega) - \varepsilon_\infty\} = \frac{\varepsilon''(\omega)}{\varepsilon'(\omega) - \varepsilon_\infty} \approx \frac{1}{Q} \tag{18}$$

for the permittivity expressed as

$$\varepsilon(\omega) = \varepsilon'(\omega) + j\varepsilon''(\omega) = \varepsilon_{ref}\left(-j\frac{\omega}{\omega_{ref}}\right)^{n-1} + \varepsilon_\infty. \tag{19}$$

$\varepsilon'(\omega)$ and $\varepsilon''(\omega)$ are the real and imaginary components of the complex permittivity function, respectively. These are frequency dependent quantities in a constant-Q model, while for nonattenuating media the real part is often considered to be constant. The parameter n takes a value between 0 and 1, ε_∞ is the high-frequency permittivity, ω_{ref} is a reference angular frequency and ε_{ref} is a corresponding reference permittivity. The relationship between n and Q is

$$n = \frac{2}{\pi}\tan^{-1}(Q). \tag{20}$$

With respect to the analytical response of a FMCW radar, the attenuating and dispersive transfer function takes the following form in frequency domain:

$$H_i(\omega) = e^{k(\omega)t_i v_i}. \tag{21}$$

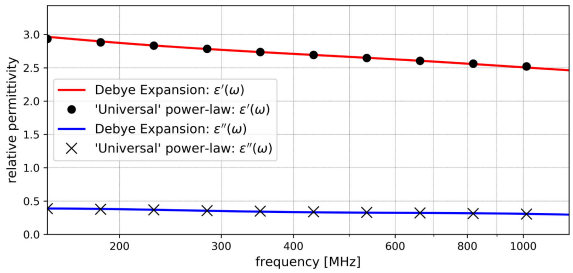

Fig. 5. Two-pole Debye function fit to a "universal" power-law dielectric model. In red and blue are the fitted real and imaginary parts of the permittivity, while circles and crosses are the corresponding data points of the dielectric model according to "overburden" in Fig. 6.

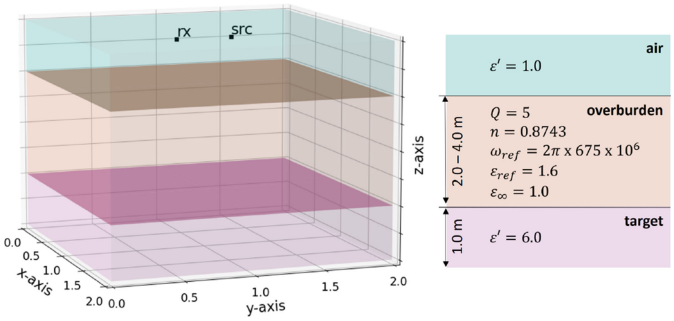

Fig. 6. Model and parameters used in simulation. Source (src) and receiver (rx) are inside of the of the upper air layer, separated by 0.4 m in y-direction and elevated 0.57 m from layer underneath. Overburden is an attenuating and dispersive constant-Q medium with $Q = 5$ and 2.0–4.0 m thickness. Half space target layer is a no-loss medium with permittivity $\varepsilon' = 6.0$ and thickness 1.0 m. Not shown in figure are the absorbing boundary conditions applied at all faces of the model space to constrain artificial reflections.

The sign of the exponent is determined by the complex permittivity convention used in (19), and the exponent is defined in terms of each reflection's two-way traveltime delay t_i, the corresponding average propagation velocities v_i, and the complex wavenumber

$$k(\omega) = j\frac{\omega}{c}\sqrt{\varepsilon(\omega)} \tag{22}$$

where c is the speed of light in vacuum.

For FDTD-simulations, permittivities following the "universal" power-law can be implemented through a multiple pole Debye formulation [18]. Fig. 5 displays the two-pole Debye approximation to a constant-Q dielectric medium.

Modeling results and analytic estimates are compared in a simple scenario with a constant-Q medium overburden and a half-space target layer below, Fig. 6. Dielectric media parameters are also listed in the figure. To assess changes in the reflected signals and their target responses, caused by increasing propagation distance in the attenuating overburden, depth to the target is increased from 2.0 to 4.0 m and reflections at different depths are analyzed individually. The half-space target is itself a 1.0 m deep layer, but only reflections from the interface between the media are fully recorded as perfectly matched layer boundaries restrain reflections from the sides of the model. 3-D FDTD-simulations are conducted as in the Method Section D, with lateral dimensions of the model equal 2.0 m $\times$ 2.0 m.

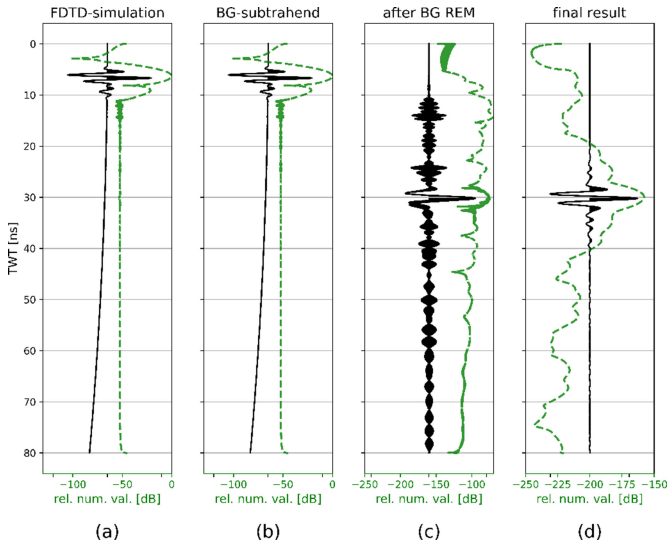

Fig. 7. Modeling corrections applied to FDTD-simulations over target depth at 2.0 m. Traces in black are displayed with a t^2 gain. In green are corresponding envelopes, being equal the magnitude of a complex signal where the real part is the trace and the imaginary part is calculated using the Hilbert transform. The envelope is plotted in dB according to the relative numeric value (rel. num. val.), referenced to the largest computed value. In (a) is the raw result from FDTD-simulations. The background subtrahend is plotted in (b), equal a simulation over a model without target layer. The recording include both the direct wave and surface reflection, as well as source effects and ringing from model boundary reflections. In (c) is the result after background removal, where high frequency noise is dominant. In (d) is the final result after frequency domain operations.

As an example of the correction steps employed, we take a look at the 2.0 m target depth simulation, Fig. 7(a). The background removal subtrahend in (b) includes the direct wave and the first reflection from the air–surface boundary. Choosing this background model was seen to be an efficient way of isolating the low amplitude target reflection, both from source effects and "ringing" caused by inadequately damped reflections at the model boundaries. The relatively strong surface reflections will also get strong sidelobes after incorporation of the instrument correction, which could drown out any low amplitude signal. As seen in (c), high frequency noise has been introduced after the subtraction due to comparably low numerical values in the target reflection. The noise is later removed when applying the amplitude taper that acts like a band-pass filter over the radar bandwidth. The instrument correction and amplitude taper are as in Fig. 3, and corrected modeling result is presented in (d).

B. Accuracy of Modeling in Attenuating and Dispersive Media

For each reflection in Fig. 8(a), the target response is seen to be fairly constant, primarily defined by the instrument correction and amplitude taper. There are, however, several characteristic and detectable features caused by attenuation of higher frequency components in a constant-Q medium. The envelopes in (b) show slight broadening with increasing propagation distance, as seen for three selected target depths (2.0 m, 3.0 m, and 4.0 m). Mainlobe widths and sidelobe strengths are similar for modeling and analytical estimates with a relative error below 12%. Associated centre frequency shifts are presented in (c),

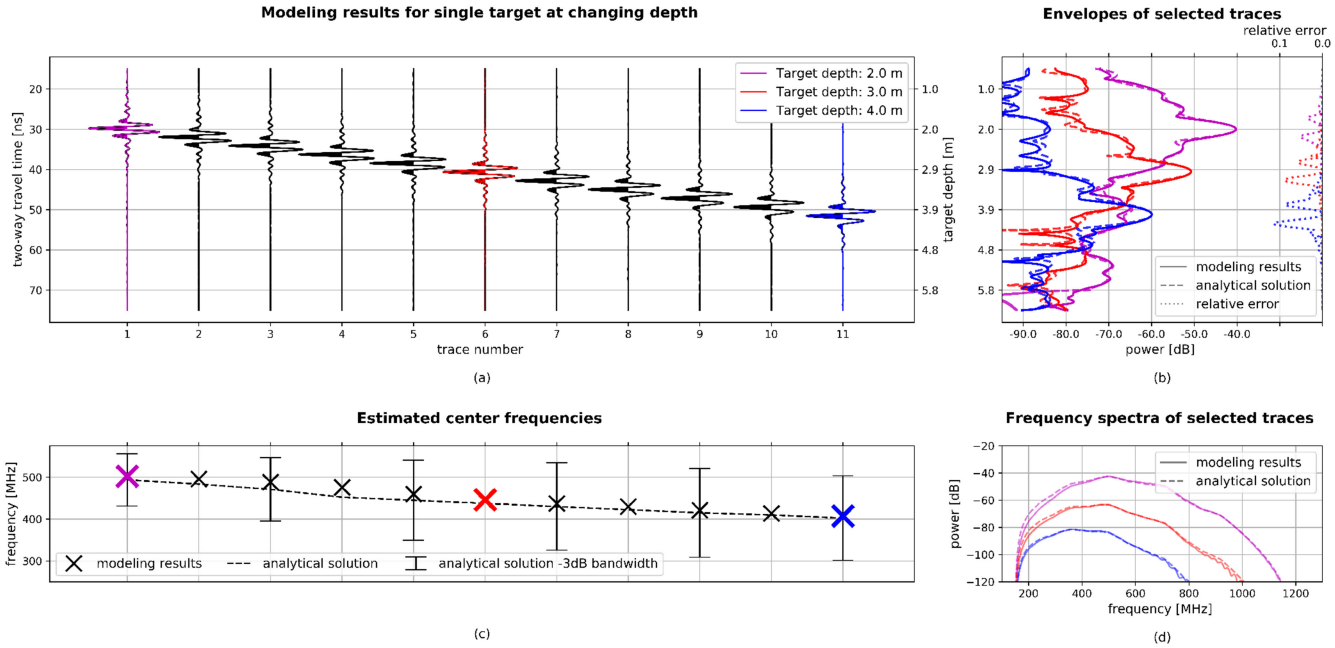

Fig. 8. (a) Results from corrected FDTD-simulations for reflector depths between 2.0 and 4.0 m. Selected traces in color corresponds to target depths at 2.0 m (magenta), 3.0 m (red), and 4.0 m (blue). All traces have normalized amplitudes. (b) Envelopes of selected traces, comparing modeling results with analytical solutions. As in Fig. 7, envelopes are calculated using the Hilbert transform. On the right side are corresponding relative errors with respect to the analytical solution's peak amplitude. (c) Estimates of center frequencies, calculated from the mean value at −3 dB below the spectrum peak. Also shown are the −3 dB bandwidth of the analytical spectra. (d) Comparison of frequency spectra for selected traces.

where modeling and analytical estimates show similar trends. A small mismatch is observed, partly due to a simple definition of the the centre frequency as the mean value at −3 dB below the spectrum peak. Looking at entire frequency spectra in (d), an overall good match is observed.

The observed differences could be caused by inaccurate FDTD-simulations, artifacts from subsequent corrections, or a combination. By looking at the relative error in (b), an inverse proportionality is observed with the amplitude of the reflected waveform, possibly indicating inaccurate representation of very small numerical values. This could for example occur during the background removal, when high frequency noise is introduced, or during the deconvolution operation. Alternatively, the FDTD-model introduce small errors that increase with propagation distance.

The geometry in this simple numerical experiment should not introduce any noticeable errors. Likewise, discrete Fourier transforms and spectral edits are likely not the source of the errors, since both the analytical solution and the modeling corrections are subjected to the same operations. The FDTD-scheme is also solved within requirements of a stable solution [7], ensuring that results are valid with numerical dispersion contained at a minimum. Therefore, inaccuracies deriving from FDTD-computations conducted with double precision should be smaller than the observed differences. Furthermore, approximating the dielectric model through multiple pole Debye formulations have also shown to give accurate results in FDTD simulations [18].

The method presented in this study describes modeling with a short-duration broadband waveform, but how to choose the optimal waveform to excite FDTD-simulations and for conducting subsequent deconvolution, is not within the scope. In fact, excitation could be carried out with a single time increment impulse to yield the reflectivity series directly and omitting the need for deconvolution [13], but then appropriate care would be required to filter out high frequency components not adhering to the FDTD-discretization requirement. This could be handled when applying the amplitude taper during the correction steps, though it might be preferable to excite simulations with a waveform for better control of the FDTD output before applying corrections. Regardless, the observed errors in Fig. 8 are minor, but an optimal waveform could perhaps reduce FDTD source artefacts that can not be fully corrected for by the background removal, as well as restrain potential inaccuracies deriving from the following deconvolution operation.

C. *RIMFAX Field Test Measurements*

To assess how well modeling replicate actual RIMFAX soundings, we look at a radargram acquired during an instrument field test survey. The comparison is also an example of how forward modeling can be used to analyze and verify subsurface properties. Field measurements were conducted with an uncalibrated RIMFAX engineering model, so the analysis will be focused on spectral characteristics in the data since power estimates would not be accurately retrieved.

Fig. 9(a) contains the map view over a selected survey line from Coral Pink state park in Utah, US. The park contains eolian deposited, migrating sand dunes [19], and we look at radar soundings acquired along a 20 m long decent from a ∼4 m tall

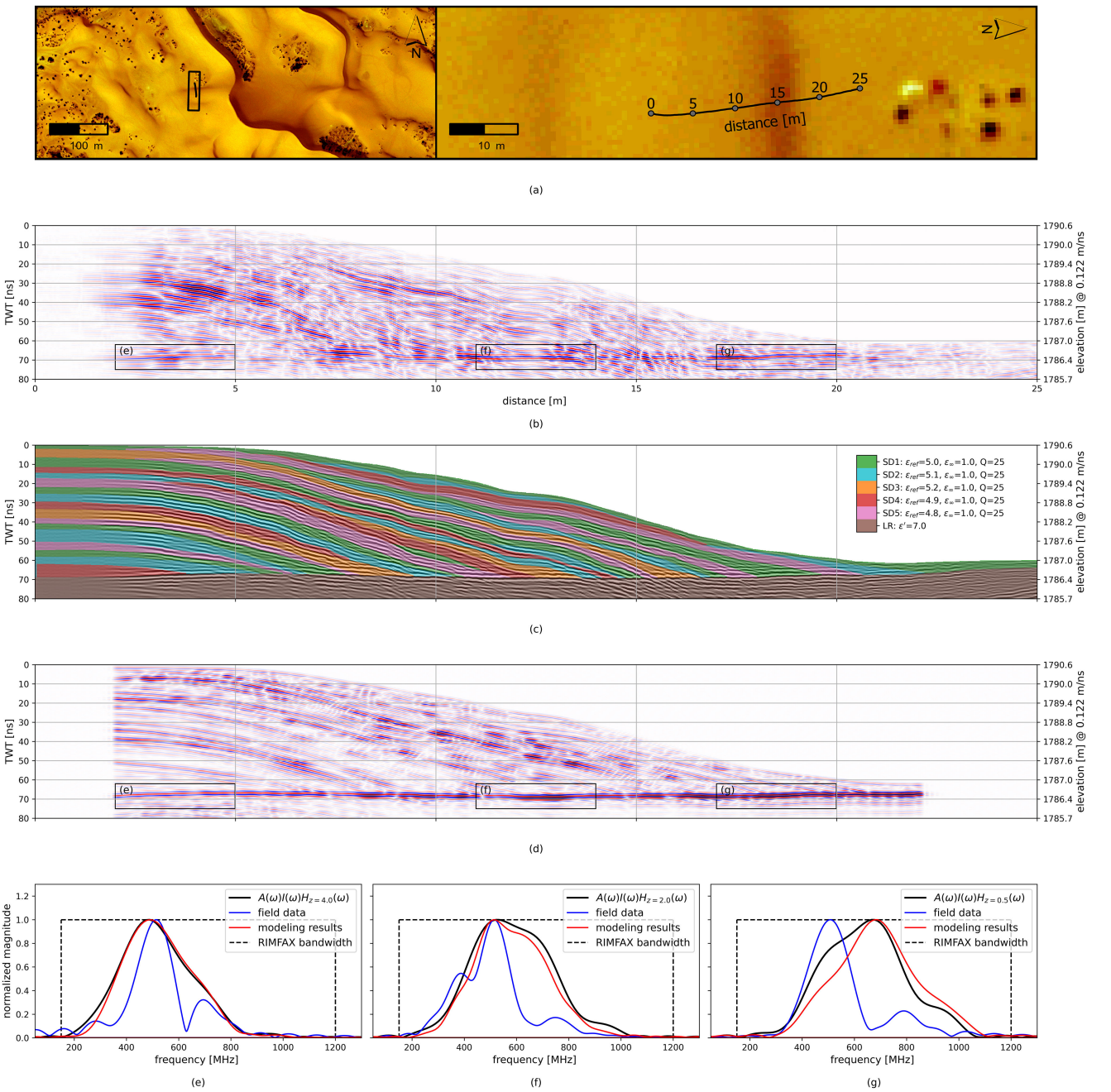

Fig. 9. (a) Selected traverse from the 2018 Coral Pink RIMFAX field test survey, plotted on top of areal imagery acquired the same year by the National Agriculture Imagery Program [22]. To the left is an overview of the nearby sand dunes and the location of the traverse. To the right is the traverse seen descending down from a single sand dune, which can be identified by elongated E-W striking shadows in the areal imagery. (b) Topography corrected radargram showing clearly the shape of the sand dune, and internal layering show down-lapping onto a semihorizontal LR. (c) Subsurface model used in FDTD-simulations. Dielectric models for sand dune layers (SD1–SD5) and LR are listed to the right. The constant-Q models for SD1–SD5, all use the same reference angular frequency, $\omega_{\text{ref}} = 2\pi \times 675 \times 10^6$. (d) Modeling results from FDTD-simulations and subsequent corrections. (e, f, g) Comparison of the frequency spectra for the field data, modeling results and theoretical estimates. Spectra are calculated within windows as shown in (b) and (d), and correspond to average depths of 4, 2, and 0.5 m, respectively. The RIMFAX bandwidth is also outlined for reference.

sand dune and onto an underlying bedrock. In the radargram in (b), internal layering within the sand dune is seen down-lapping onto a semiplanar lower reflector (LR), interpreted as the continuation of the flat bedrock terrain outcropping to the north of the dune. In what follows, we will show how modeling can be used to reproduce similar target responses as in the recorded field data, which is determined by the dune's internal structure and properties. However, an in-depth analysis of the radargram and description of how soil and subsurface parameters are determined, are not within the scope of this study.

The first steps of processing the radargram was done according to Fig. 1(a), with the amplitude taper from Fig. 3. Thereafter, a background removal subtracted a moving average from each sounding, with the average calculated within a window

length of 5 m. The radar system's gating effects [5] were compensated for by equalizing the received power, and a gain with depth was applied in order to visually enhance weaker reflections. Each sounding were shifted vertically so that the peak of the surface reflection would coincide with time zero, before applying a topography correction aligning each sounding according to the elevation and a constant subsurface velocity of 0.122 m/ns. The velocity was initially chosen so that the strong, lower reflection got more planar with an horizontal orientation.

The FDTD subsurface model presented in Fig. 1(c), uses the field data radargram directly as an outline, where the depth axis is linearly related TWT through the constant subsurface velocity. The LR was mapped by tracing the peak of the signal's envelope along the traverse, and interpolating in between where its presence is less clear. Power estimates are not assessed in this study, nor are reflections within the lower layer, so it was simply assigned an arbitrary constant permittivity value, $\varepsilon' = 7$.

Digitizing layering within the sand dune was done by tracing the most prominent reflections, decided to be those with a considerable lateral extent of at least a couple of meters. For simplicity during this assessment, reflections in the processed radargram are assumed to be due to subsurface reflectors, regardless if they in fact could be artificial due to the background removal processing. Furthermore, radargram migration would be required if an exact representation of the reflector dip would be necessary, but not considered significant in this assessment. The mapped reflections were then defined as top interfaces of layers which were assigned a range of dielectric values around a mean velocity of 0.134 m/ns, or $\varepsilon' = 6$, at the center frequency 675 MHz. We define all these layers to have the same constant-Q dielectric model, with $Q = 25$ as an initial guess. Dielectric parameterization is summarized in Fig. 9(c). All media are considered nonmagnetic.

The radargram in Fig. 9(d) was created by running FDTD-simulations over the subsurface model as described for Fig. 8. The 2-D-subsurface model extend in cross-track direction to a 2.5D model, and each sounding was computed every 10 cm along the traverse within a $4.0 \times 1.5 \times 5.5$ m^3 subset [20]. At last, corrections were applied according to Fig. 1(b).

Qualitatively, the modeled radargram contain most of the prominent features from the field data, like the sand dune's internal layering down-lapping onto a lower, planar reflection. The field data, however, inevitably contain more details and more incoherent reflections than the simulation over a simplified and orderly stratified FDTD-model. Target responses along the lower planar reflection seem nevertheless to be fairly similar the two cases.

To assess how well modeling replicate field measurements, in Fig. 9(e)–(g), spectra are compared at depths of $\sim$4, $\sim$2, and $\sim$0.5 m. This is also an example of how to use a boundary reflector to evaluate overburden properties. A edge tapered cosine window (tukey window) is multiplied with targeted data ranges in time-domain, outlined in (b) and (d), before transforming into frequency-domain. Analytical estimates are added for reference, equal the product of the instrument correction, amplitude taper, the transfer function in (21), and similar window taper effects.

The spectra of the modeling results are aligned with analytical estimates, while the field data spectra have a different appearance with, e.g., a prominent dip at around 650 MHz. Still, for the most part, the field data spectra are contained within the others. The apparent mismatch for the $\sim$0.5 m depth in (g), is mostly because the analytic and modeling are normalized to their peak at 650 MHz while the field data are normalized to a peak value of 500 MHz, due to the dip in frequency content. Nevertheless, by looking at the trend in frequency shift with overburden thickness, forward modeling confirm that field measurements are fairly well described by a constant-Q approximation with $Q = 25$.

Using the boresight gain as an approximation to the instrument correction is a simplified approach, as it ideally should also take into account radar electronics that is causing the prominent dip in the field data spectra at around 650 MHz. Interference form the survey vehicle could also be significant and should ideally be incorporated as well. Assessment has been made for integration with the Mars 2020 rover [21], but has not been studied for field test vehicles. When studying RIMFAX data from Mars, however, all effects described by the instrument correction will be attempted corrected for during data processing, meaning that only the amplitude taper will be necessary during FDTD-modeling corrections. This would in fact be preferable for GPR imaging and analysis, as instrument effects will only increase sidelobes of waveforms and reduce the vertical resolution in the radargram.

IV. Conclusion

We have demonstrated that it is possible to conduct FDTD-simulations with a short-duration waveform and model the same target response as would be acquired by a FMCW radar with a stretch processing receiver. Special considerations necessary for modeling weak reflections in realistic, attenuating, and dispersive media have been carefully reviewed. Comparison with field test measurements has assessed the accuracy of the modeling approach and demonstrated the practical use. Forward modeling could therefore be useful for future in-detail analysis of data acquired with RIMFAX, appraising how subsurface structures are imaged with the radar system's resolution and how frequency-dependent attenuation modifies received signals. For example, measurements of the Martian subsurface could be compared with forward modeling over hypothetical subsurface models, and analyzed in a similar way as have been done in lunar exploration. Studying the combined effects of dielectric and volume-scattering losses is furthermore an interesting application, and attempting to decouple these into their individual contributions may in turn be helpful when searching for subsurface water content. Perhaps will it be possible to detect or infer water content in the subsurface through a particular dielectric relaxation. Moreover, the forward modeling approach presented in this study may also turn out to be valuable for inversion modeling. By having obtained the target response of a specific radar system, forward modeling could be compared directly with soundings acquired over a subsurface with unknown properties, with an iterative optimization of FDTD-model parameters.

ACKNOWLEDGMENT

The authors would like to acknowledge RIMFAX team members responsible for the 2018 Coral Pink field test survey, and especially Tor Berger who made the recordings available for us to present in this publication.

REFERENCES

[1] E. Pettinelli, S. E. Lauro, E. Mattei, B. Cosciotti, and F. Soldovieri, "Stratigraphy versus artefacts in the Chang'e-4 low-frequency radar," *Nature Astron.*, vol. 5, pp. 890–893, 2021.
[2] C. Li *et al.*, "Pitfalls in GPR data interpretation: False reflectors detected in lunar radar cross sections by Chang'e-3," *IEEE Trans. Geosci. Remote Sens.*, vol. 56, no. 3, pp. 1325–1335, Mar. 2018.
[3] J. Lai *et al.*, "First look by the Yutu-2 rover at the deep subsurface structure at the lunar farside," *Nature Commun.*, vol. 11, no. 1, 2020, Art. no. 3426.
[4] L. Zhang *et al.*, "Simulation of the lunar regolith and lunar-penetrating radar data processing," *IEEE J. Sel. Topics Appl. Earth Observ. Remote Sens.*, vol. 11, no. 2, pp. 655–663, Feb. 2018.
[5] S.-E. Hamran *et al.*, "Radar imager for Mars' subsurface experiment-RIMFAX," *Space Sci. Rev.*, vol. 216, no. 8, pp. 1–39, 2020.
[6] D. B. Davidson, *Computational Electromagnetics for RF and Microwave Engineering*. 2nd ed. Cambridge, U.K.: Cambridge Univ. Press, 2010.
[7] C. Warren, A. Giannopoulos, and I. Giannakis, "gprMax: Open source software to simulate electromagnetic wave propagation for ground penetrating radar," *Comput. Phys. Commun.*, vol. 209, pp. 163–170, 2016.
[8] G. Turner and A. F. Siggins, "Constant Q attenuation of subsurface radar pulses," *Geophysics*, vol. 59, no. 8, pp. 1192–1200, 1994.
[9] F. Hollender and S. Tillard, "Modeling ground-penetrating radar wave propagation and reflection with the Jonscher parameterization," *Geophysics*, vol. 63, no. 6, pp. 1933–1942, 1998.
[10] M. Bano, "Constant dielectric losses of ground-penetrating radar waves," *Geophys. J. Int.*, vol. 124, no. 1, pp. 279–288, 1996.
[11] B. Keel, J. Baden, W. Melvin, and J. Scheer, "Advanced pulse compression waveform modulations and techniques," in *Principles of Modern Radar: Advanced Techniques*, Edison, New Jersey: SciTech Publishing, 2012, pp. 19–85.
[12] G. F. Margrave, "Theory of nonstationary linear filtering in the fourier domain with application to time-variant filtering," *Geophysics*, vol. 63, no. 1, pp. 244–259, 1998.
[13] D. T. Murphy, A. Southern, and L. Savioja, "Source excitation strategies for obtaining impulse responses in finite difference time domain room acoustics simulation," *Appl. Acoust.*, vol. 82, pp. 6–14, 2014.
[14] D. Stillman and G. Olhoeft, "Frequency and temperature dependence in electromagnetic properties of martian analog minerals," *J. Geophys. Res., Planets*, vol. 113, no. E9, 2008, doi: 10.1029/2007JE002977.
[15] Y. Brouet, P. Becerra, P. Sabouroux, A. Pommerol, and N. Thomas, "A laboratory-based dielectric model for the radar sounding of the martian subsurface," *Icarus*, vol. 321, pp. 960–973, 2019.
[16] P. G. Richards and K. Aki, *Quantitative Seismology: Theory and Methods*. vol. 859. New York, NY, USA: Freeman, 1980.
[17] A. K. Jonscher, "The 'universal' dielectric response," *Nature*, vol. 267, no. 5613, pp. 673–679, 1977.
[18] I. Giannakis, A. Giannopoulos, and N. Davidson, "Incorporating dispersive electrical properties in FDTD GPR models using a general Cole-Cole dispersion function," in *Proc. IEEE 14th Int. Conf. Ground Penetrating Radar*, 2012, pp. 232–236.
[19] R. Ford, S. Gillman, D. Wilkins, W. Clement, and K. Nicoll, "Geology and geomorphology of coral pink sand dunes state park," *Utah Geological Assoc. Pub.*, vol. 28, pp. 379–406, 2010.
[20] S. Eide, S.-E. Hamran, H. Dypvik, and H. E. F. Amundsen, "Ground-penetrating radar modeling across the Jezero crater floor," *IEEE J. Sel. Topics Appl. Earth Observ. Remote Sens.*, vol. 14, pp. 2484–2493, 2021.
[21] E. Gonzales, E. Cordoba, and S.-E. Hamran, "Compatibility tests between the mars vehicle system test bed and RIMFAX radar antenna prototype for the Mars 2020 mission," in *Proc. IEEE Int. Symp. Electromagn. Compat. Signal/Power Integrity*, 2017, pp. 44–50.
[22] USDA-FPAC-BC-APFO Aerial Photography Field Office, "NAIP digital georectified image geospatial_data_presentation_form: Remote-sensing image," *Entity ID: M_3711259_SW_12_060_20180807*, 2019. Accessed: Nov. 15, 2021. [Online]. Available: https://earthexplorer.usgs.gov

Sigurd Eide received the M.Sc. degree in geophysics from the University of Oslo, Oslo, Norway, in 2014. He is currently working toward the Ph.D. degree in geophysics with the Department of Technology Systems, University of Oslo.

From 2014 to 2018, he was a Consultant within marine geophysics and geographical information systems. Since 2018 and the start of his Ph.D. work, he has been engaged with the RIMFAX instrument on the NASA Mars 2020 Perseverance Rover Mission, where he has been developing methods of data analysis and taking part in tactical payload operation. His research interests includes remote sensing and numerical modeling applied to geological exploration, in particular ground penetrating radar and active-source seismic.

Titus Casademont received the M.Sc. degree in geophysics from the University of Hamburg, Hamburg, Germany, in 2020. He is currently working toward the Ph.D. degree in geophysics with the Center for Space Sensors and Systems, University of Oslo, Oslo, Norway.

As a member of the Mars 2020 RIMFAX team, he studies dielectric permittivity and density inversion of the Martian subsurface, both with conventional and machine learning approaches. His research interests are centered around radar remote sensing for earth and planetary geoscience with a focus on *in situ* UWB radar.

Øyvind Lund Aardal received the M.Sc. degree in applied mathematics from the University of Oslo, Oslo, Norway, in 2008, and the Ph.D. degree in medical radar from the University of Oslo, in 2013.

Since 2020, he has been an Adjunct Associate Professor with the Department of Technology Systems, University of Oslo, where he teaches a course in radar remote sensing. Since 2009, he has been a Scientist with the Norwegian Defence Research Establishment (FFI), Norway. His research interests include radar signal processing, medical radar, and sensor data handling and exploitation.

Svein-Erik Hamran received the M.Sc. degree in physics from the Norwegian University of Science and Technology, Trondheim, Norway, in 1984, and the Ph.D. degree in physics from the University of Tromsø, Tromsø, Norway, in 1990.

He is currently a Professor with the Department of Technology Systems, University of Oslo. He is also the Principal Investigator of the Radar Imager for Mars subsurface eXperiment RIMFAX on the NASA Mars 2020 Perseverance Rover Mission and a Co-Principal Investigator on the WISDOM GPR experiment on the ESA ExoMars rover. His research interests include UWB radar design, radar imaging, and modeling in medical and ground-penetrating radar.